Supplementary Information

Revealing the Structure-Activity Relationship of Two Cu-porphyrin-based Metal-Organic Frameworks for the Electrochemical CO_2-to-HCOOH Transformation

Meng-Jie Liu[1], Si-Min Cao[1], Bao-Qi Feng, Bao-Xia Dong*, Yan-Xia Ding, Qiu-Hui Zheng, Yun-Lei Teng*, Zong-Wei Li, Wen-Long Liu, Li-Gang Feng

School of Chemistry and Chemical Engineering, Yangzhou University, Yangzhou 225002, Jiangsu, China

*Corresponding authors.

E-mail addresses: bxdong@yzu.edu.cn (B-X. Dong), ylteng@yzu.edu.cn (Y.-L. Teng)

[1] These authors contributed equally to this work.

15. **Figure S8.** CV curves of (a) PCN-222(Cu); (b) PCN-224(Cu); (c) Cu-TCPP in the region of –0.8 ~ –0.9 V vs. Ag/AgCl at various scan rate (5 ~ 40 mV/s); (d) Current density plots at various scan rates.
16. **Figure S9.** (a) Steady-state current density and (b) the selectivity for each gas product in a potential range from −0.4 to −0.9 V vs. RHE of PCN-222(Cu)/C, PCN-224(Cu)/C and Cu-TCPP/C.
17. **Table S8.** Long-term chronoamperograms and product quantified results for three catalysts
18. **Table S9.** Performance of some Cu-related electrocatalysts in reference for transformation of CO_2 to HCOOH
19. **Figure S10.** Chromatographic peak and standard curve for pure hydrogen and CO established on TDX-01 column for GC analysis.
20. **Figure S11.** Chromatographic peaks and standard curves for pure methanol and ethanol established on PEG-20M column for GC analysis.
21. **Figure S12.** Chromatographic peak and standard curve for $COOH^-$ established on high-end ion chromatography.

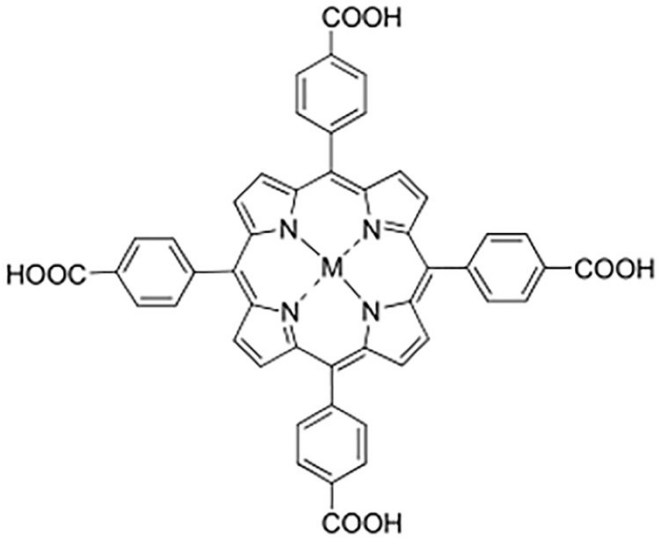

Figure S1. The molecular structure of the Cu-TCPP ligand.

Table S1. Structural comparisons between PCN-222(Cu) and PCN-224(Cu)

Name	PCN-222(Cu)	PCN-224(Cu)
Molecular formula	$Zr_6O_8(OH)_8[TCPP\text{-}Cu]_2$	$Zr_6O_{12}(OH)_8[TCPP\text{-}Cu]_{1.5}$
M (g mol^{-1})	2516.03	2139.74
n (mol) for 10 mg	$3.97*10^{-6}$	$4.67*10^{-6}$
Zr_6 : Cu-TCPP	1:2	1:1.5
BET ($m^2\ g^{-1}$)	1900 (reported value of 2312)	1690 (reported value of 2285)
Pore diameter (nm)	1.2, 3.2	1.3, 1.6

V (cm^3 g^{-1})	1.18 (reported value of 1.39)	1.107 (reported value of 1.095)
Color and shape	red, needle	red, cubic
Crystal system	hexagonal system	cubic system
Cell parameters	*a*=*b*=41.968(7) Å *c*=17.143(2) Å *α*=*β*=90° *γ*=120°	*a*=*b*=*c*=38.512(2) Å *α*=*β*=*γ*=90°
Space groups	*P*6/mmm	*Im*-3*m*
Z	6	4

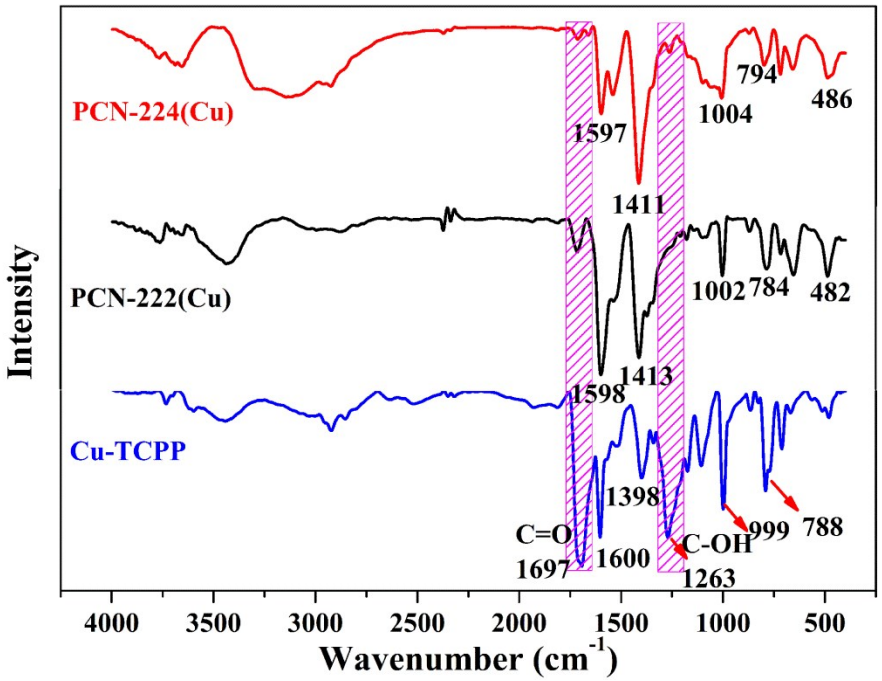

Figure S2. IR spectrum of each catalyst.

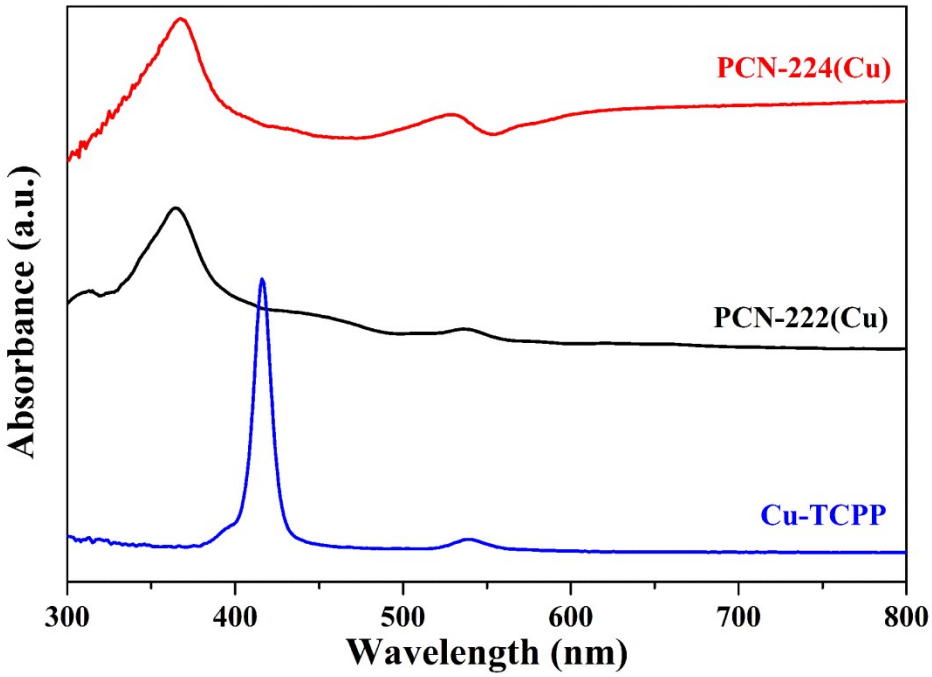

Figure S3. UV-vis spectrum of each catalyst in CH_2Cl_2.

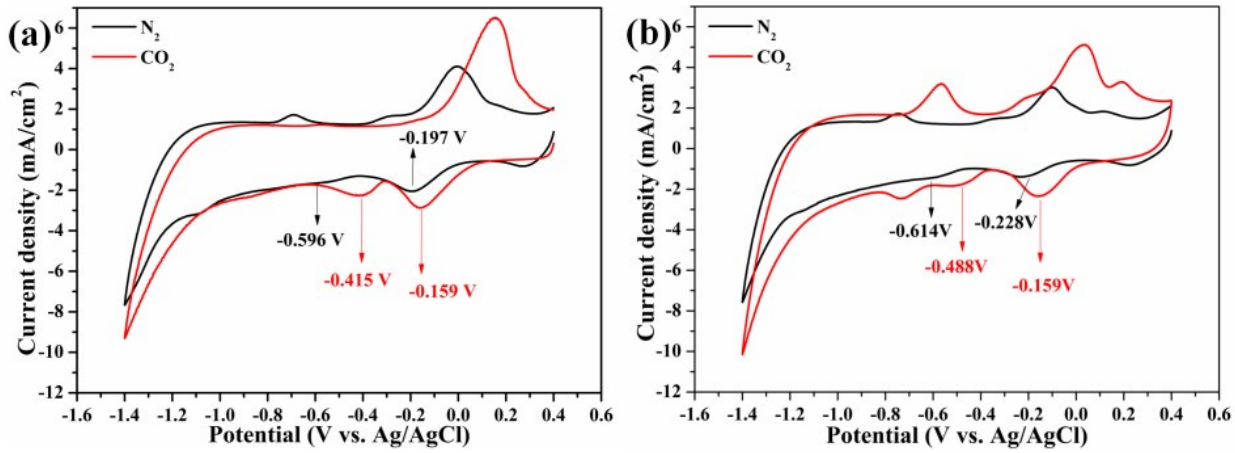

Figure S4. CVs of (a) PCN-222(Cu)/C and (b) PCN-224(Cu)/C loaded on CP in N_2 and CO_2-saturated electrolyte (vs. Ag/AgCl).

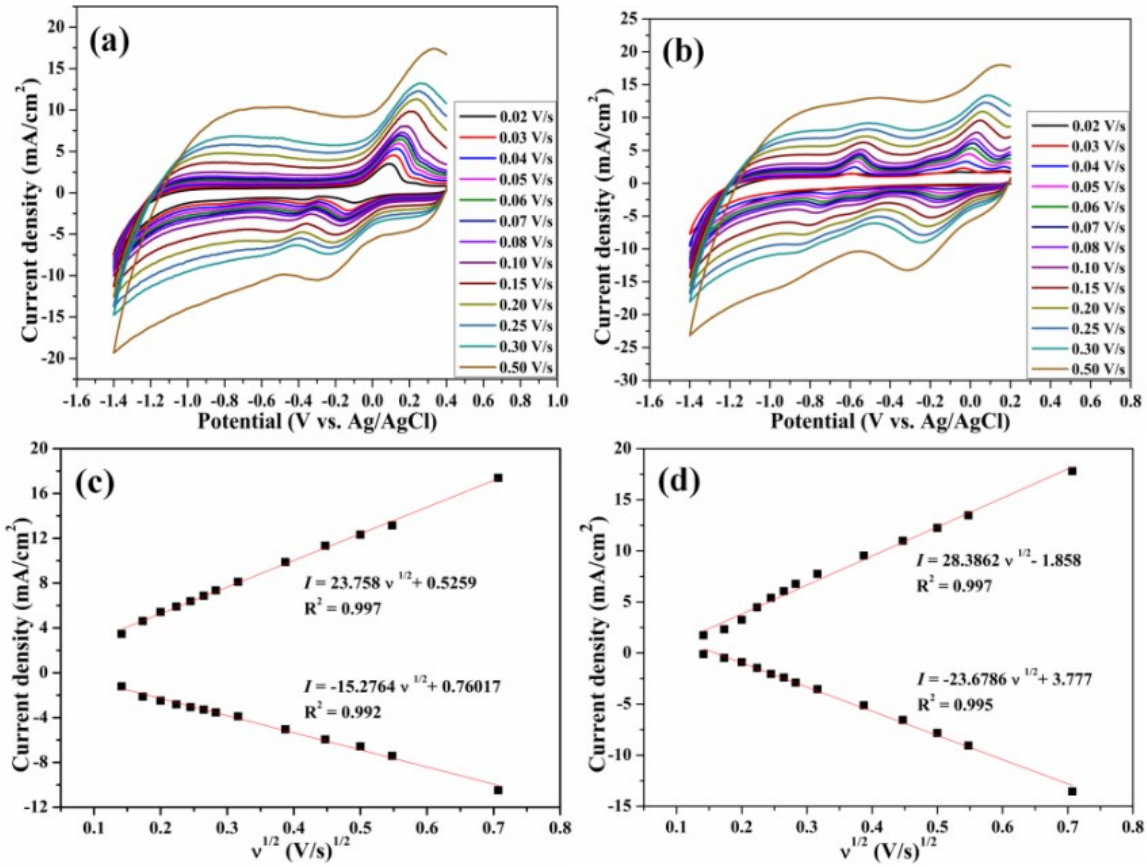

Figure S5. CVs and peak current intensity variations of (a) PCN-222(Cu)/C and (b) PCN-224(Cu)/C in a CO_2-saturated electrolyte as the scan rate is systematically increased from 0.02 to 0.5 V/s; Dependence of cathodic and anodic peak currents of the $Cu^{II/I}$ redox waves versus the scan rate, (c) PCN-222(Cu)/C, (d) PCN-224(Cu)/C.

Table S2. The surface concentration (Γ) of the electroactive substance and the utilization percentage of Cu-TCPP, PCN-222(Cu) and PCN-224(Cu)

	Cu-TCPP	PCN-222(Cu)	PCN-224(Cu)
n (mol)	2.35×10^{-6}	7.95×10^{-7}	9.35×10^{-7}
Γ (mol cm^{-2})	2.38×10^{-8}	3.16×10^{-8}	2.86×10^{-8}
Utilization percentatage (%)	2.02	7.95	6.12

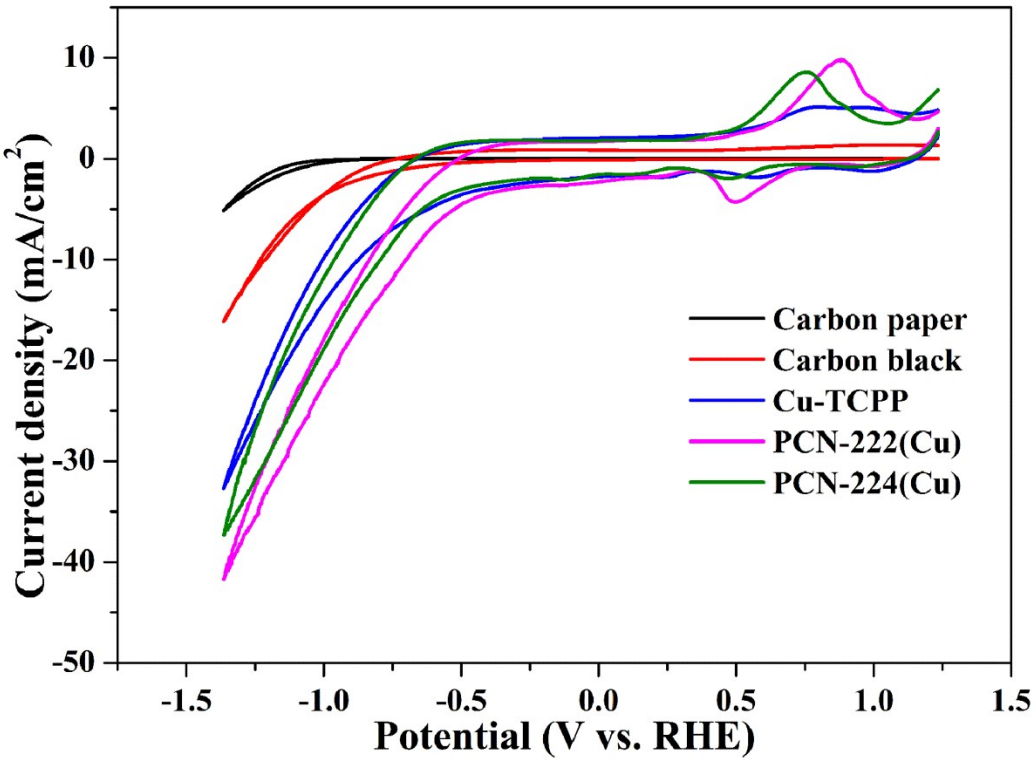

Figure S6. Comparisons of CVs for bare CP electrode, carbon black, Cu-TCPP/C, PCN-222(Cu)/C, and PCN-224(Cu)/C loaded on the CP electrode in CO_2-saturated electrolyte in the potential range −1.4 ~ 1.2 V vs. RHE.

Table S3. Chronoamperograms and product quantified result for PCN-222(Cu)/C

PCN-222(Cu)/C						
vs. Ag/AgCl (V)	-1.035	-1.135	-1.235	-1.335	-1.435	-1.535
vs. RHE (V)	-0.4	-0.5	-0.6	-0.7	-0.8	-0.9
η_{HCOOH} (mV)	150	250	350	450	550	650
j (mA cm^{-2})	0.16	0.69	1.24	3.22	5.87	9.53
Q (C)	2.269	9.898	17.81	46.31	84.48	137.3
FE_{H2} (%)	58.97	62.51	54.8	50.67	65.21	71.56
FE_{CO} (%)	14.17	8.95	3.18	5.2	2.85	2
C_{HCOOH} (ppm)	0.93	7.407	21.685	81.48	108.31	148.07
FE_{HCOOH} (%)	10.31	18.82	30.62	44.25	32.24	27.12
n_{HCOOH} (mol)	1.21×10^{-6}	9.66×10^{-6}	2.83×10^{-5}	1.06×10^{-4}	1.41×10^{-4}	1.93×10^{-4}
TON (n_{HCOOH}/n)	1.52	12.15	35.6	133.33	177.36	242.77
TOF (h^{-1})	0.76	6.08	17.8	66.67	88.68	121.39

Table S4. Chronoamperograms and product quantified result for PCN-224(Cu)/C

PCN-224(Cu)/C						
vs. Ag/AgCl (V)	-1.035v	-1.135v	-1.235v	-1.335v	1.435v	1.535v
vs. RHE (V)	-0.4	-0.5	-0.6	-0.7	-0.8	-0.9
η_{HCOOH} (mV)	150	250	350	450	550	650
j (mA cm^{-2})	0.181	0.651	1.22	2.376	2.91	6.775
Q (C)	2.602	9.371	17.5	34.21	41.85	97.56
FE_{H2} (%)	51.78	58.04	56.61	59.78	73.49	67.24
C_{HCOOH} (ppm)	1.383	8.944	22.195	46.43	34.61	103.92
FE_{HCOOH} (%)	13.37	24	31.9	34.14	20.8	26.79
n_{HCOOH} (mol)	1.8×10^{-6}	1.17×10^{-5}	2.9×10^{-5}	6.1×10^{-5}	4.51×10^{-5}	1.36×10^{-4}
TON (n_{HCOOH}/n)	1.93	12.51	31.02	65.24	48.24	145.45
TOF (h^{-1})	0.97	6.26	15.51	32.62	24.12	72.73

Table S5. Chronoamperograms and product quantified result for Cu-TCPP/C

Cu-TCPP/C						
vs. Ag/AgCl (V)	-1.035	-1.135	-1.235	-1.335	-1.435	-1.535
vs. RHE (V)	-0.4	-0.5	-0.6	-0.7	-0.8	-0.9
η_{HCOOH} (mV)	150	250	350	450	550	650
j (mA cm^{-2})	0.11	0.37	0.73	2.185	3.03	5.385
Q (C)	1.581	5.321	10.53	31.47	43.65	77.55
FE_{H2} (%)	32.83	61.34	63.08	41.64	61.86	70.51
FE_{CO} (%)	\	\	\	0.82	2.24	1.18
C_{HCOOH} (ppm)	\	2.685	7.27	35.52	47.23	77.4
FE_{HCOOH} (%)	\	12.69	17.36	28.38	27.21	25.1
n_{HCOOH} (mol)	\	3.5×10^{-6}	9.48×10^{-6}	4.63×10^{-5}	6.16×10^{-5}	1×10^{-4}
TON (n_{HCOOH}/n)	\	1.49	4.03	19.7	26.21	42.55
TOF (h^{-1})	\	0.75	2.02	9.85	13.11	21.28

Table S6. Correlated data in references for clarifying the CO_2 capture ability

	PCN-222-H_2 [1]	PCN-224-Zn [2]
BET surface area ($m^2\ g^{-1}$)	1728	1638.9
CO_2 uptake (273K) ($cm^3\ g^{-1}$)	58	38.3
CO_2 uptake (298K) ($cm^3\ g^{-1}$)	35	24.7
Heat of adsorption (kJ mol^{-1})	23.6	36.8

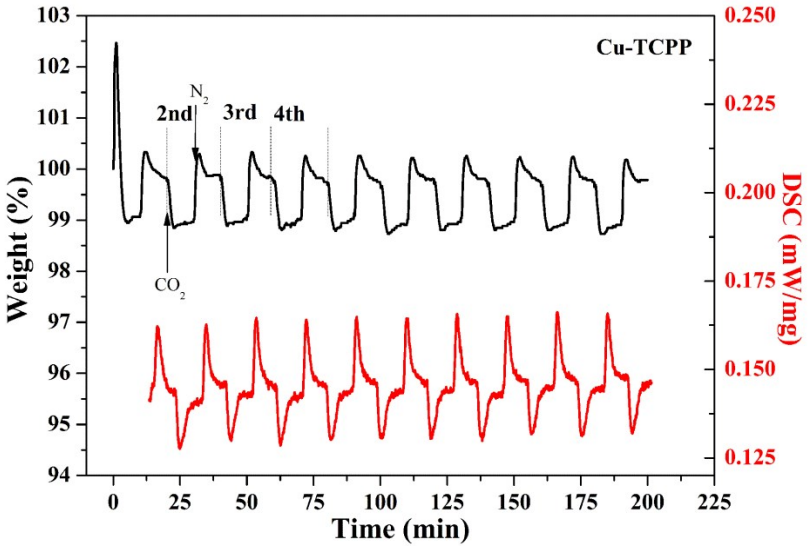

Figure S7. Gas cycling experiment for Cu-TCPP catalyst under a pure CO_2 and N_2 flow at a constant temperature of 303 K for 10 cycles.

Table S7. The obtained R_{cell} and R_{ct} in each catalyst

	PCN-222(Cu)/C	PCN-224 (Cu)/C	Cu-TCPP/C
R_{cell}	4.248	4.587	4.399
R_{CT}	10.23	10.13	15.75
C_{dl} (μF cm^{-2})	21.2	17.8	15.9
ECSA (cm^2)	1.06	0.89	0.79

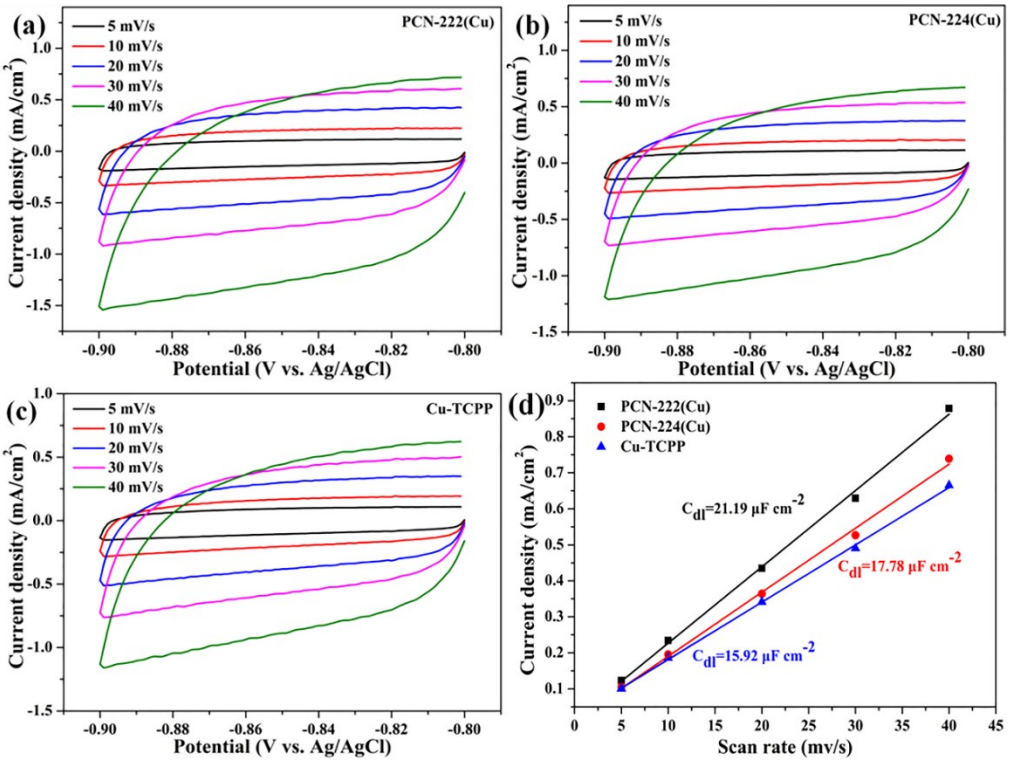

Figure S8. CV curves of (a) PCN-222(Cu); (b) PCN-224(Cu); (c) Cu-TCPP in the region of –0.8 ~ –0.9 V vs. Ag/AgCl at various scan rate (5 ~ 40 mV/s); (d) Current density plots at various scan rates.

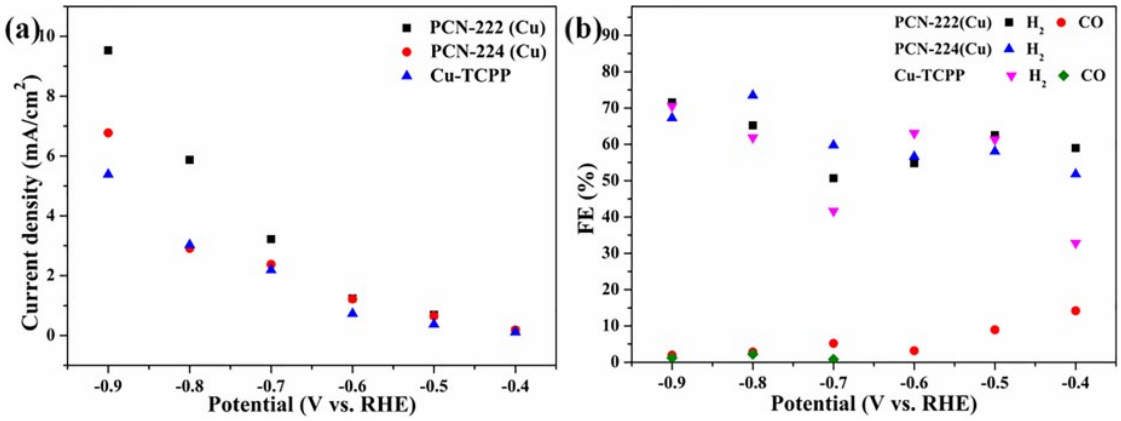

Figure S9. (a) Steady-state current density and (b) the selectivity for each gas product in a potential range from −0.4 to −0.9 V vs. RHE of PCN-222(Cu)/C, PCN-224(Cu)/C and Cu-TCPP/C.

Table S8. Long-term chronoamperograms and product quantified results for three catalysts

Catalyst	PCN-222(Cu)	PCN-224(Cu)	Cu-TCPP	PCN-222(Cu)	PCN-224(Cu)	Cu-TCPP
t (h)	2			10		
Q (C)	46.3	34.2	31.5	199.3	144.3	90.2
j (mA cm^{-2})	3.2	2.4	2.2	2.8	2.0	1.3
FE_{HCOOH} (%)	44.3	34.1	28.4	34.6	34.9	23.8
FE_{H2} (%)	50.7	59.8	41.6	51.9	58.1	60.7
FE_{CO} (%)	5.2	\	0.8	11.3	\	0.8

Table S9. Performance of some Cu-related electrocatalysts in reference for transformation of CO_2 to HCOOH

Catalyst	**Electrolyte**	**Product**	**Potential [overpotential (V)]**	***j* (mA cm^{-2})**	**FE (%)**	**Ref**
PCN-222(Cu)	0.5 M $KHCO_3$	HCOOH	–0.70 V vs. RHE [0.45]	3.2	44.25	This work
PCN-224(Cu)				2.4	34.14	
CR-MOF	0.5 M $KHCO_3$	HCOOH	–1.20 V vs. SHE [0.54]		30	3
Cu-SIM NU-1000 thin film	0.1 M $NaClO_4$	HCOOH	–0.82 V vs. RHE	1.2	28	4

$[Cu(cyclam)](ClO_4)_2$	0.1 M Bu_4NBF_4/DMF/H_2O	HCOOH	–2.0 V vs. Fc/Fc^+ [0.54]	1	90	5
Cu nanofoams	0.5 M $NaHCO_3$	HCOOH	–1.50 V vs. Ag/AgCl		37	6
Hierarchical Cu pillar	0.1 M $KHCO_3$	HCOOH	–0.50 V vs. RHE [0.68]	~1.3	28.7	7
Nano CuO	0.5 M $KHCO_3$	HCOOH	–1.40 V vs. Ag/AgCl		61	8
Amorphous Cu NPs	0.1 M $KHCO_3$	HCOOH	–1.40 V vs. Ag/AgCl	~6	37	9
Cu-Pc	0.5 M $KHCO_3$	HCOOH	–0.86 V vs. RHE		25	10
Cu_2(CuTCPP)	CH_3CN solution with 1 M H_2O and 0.5 M $EMIMBF_4$	HCOOH	-1.55V vs. Ag/Ag^+	~3	68.4	11
MOF-derived OD Cu/C-1000	0.1 M $KHCO_3$	HCOOH	−0.5 V vs. RHE [0.25]		18	12
Cu foil	0.1 M KCl	HCOOH	−1.44 V vs. NHE		6.6	13
Cu foil	0.1 M $KHCO_3$	HCOOH	−1.41 V vs. NHE		9.7	14
Cu_2O-derived Cu electrode	0.1 M $KHCO_3$	HCOOH	−0.78 V vs. RHE [0.53]	6.37	25	15
Cu (100)			−0.85 V vs. RHE [0.6]	0.97	9	
Cu (111)			−0.95 V vs. RHE [0.7]	1.18	20.8	
Cu (110)			−0.80 V vs. RHE [0.55]	1.1	24.7	
Cu_2O/Cu annealed at 500ºC	0.1 M $KHCO_3$	HCOOH	−0.45 V vs. RHE [0.25]	0.6	33	16
CuO nanowires	0.5 M $KHCO_3$	HCOOH	−1.5 V vs. Ag/AgCl [0.597]	80	38	17
Cu nanoparticles/o-CNT-NW(1%)	0.5 M $KHCO_3$	HCOOH	−2.0 V vs. Ag/AgCl [1.097]		27.5	18
Cu-CDots nanocorals	0.5 M $KHCO_3$	HCOOH	−0.7 V vs. RHE [0.45]	4.2	79	19
Cu NWs-Bi NSs	0.5 M $KHCO_3$	HCOOH	−0.86 V vs. RHE	~6.2	87	20
in situ-treated Bi/Cu foam	0.1 M $KHCO_3$	HCOOH	−1.6 V vs. Ag/AgCl	10	92	21
Sn-Cu alloy	0.5 M KCl	HCOOH	−1.14 V vs. RHE	~100	82	22
G-Cu_xO-2h	0.5 M $KHCO_3$	HCOOH	−0.8 V vs. RHE	19.3	81	23
Bi-SnO/Cu foam	0.1 M $KHCO_3$	HCOOH	−1.7 V vs. Ag/AgCl	12	93	24
$Cu_{25}In_{75}$	0.5 M $NaHCO_3$	HCOOH	−0.7 V vs. RHE	5.3	84.1	25
CuZn-0.5	0.1 M $KHCO_3$	HCOOH	−1.1 V vs. RHE	4.5	~60	26
PTFE−Cu NW	0.1 M $KHCO_3$	HCOOH	−0.6 V vs. RHE	~7.6	68	27
Pb_{ed}/Cu NWs	0.5 M $KHCO_3$	HCOOH	−0.93 V vs. RHE	~8.3	25	28

Pb_{ar}/Cu NWs				9.35	22	
nanoporous Zn-Cu	0.5 M $KHCO_3$	HCOOH	−0.9 V vs. RHE	~5.6	29	29

Experimental Section

Materials.

All chemicals used as received without further purification. The water used throughout all experiments was deionized with 18.2 MΩ from a Millipore system. Carbon monoxide (99.999%) and hydrogen (99.999%) were used for calibration.

Preparation of the Electrodes.

MOFs of PCN-222(Cu) and PCN-224(Cu) and ligand of Cu-TCPP (Figure S1) were synthesized following a process described in the literature.[30-31] After a typical hydrothermal synthesis, red hexagonal prism-shaped crystals of PCN-222(Cu), and red cubic crystals of PCN-224(Cu) were collected by filtration. Carbon paper (99.5% carbon, 1 cm × 1 cm) was treated with 6.0 M HCl overnight to remove trace metal impurity, rinsed thoroughly with Milli-Q water, and dried in a vacuum before use. 10.0 mg (3.97×10^{-6} mol) of PCN-222(Cu) and 20.0 mg carbon black (Vulcan XC-72R) were ultrasonically dispersed into 1.0 mL acetone (0.5 wt% Nafion) for 2 h to form a slurry. A 160 μL of the slurry was dropped on each surface of the carbon paper and then air-dried before use (loading of 3.0 mg cm^{-2}). PCN-224(Cu)/C (10 mg, 4.67×10^{-6} mol of catalyst) and Cu-TCPP/C (10 mg, 8.21×10^{-6} mol of catalyst) electrodes were assembled according to the same procedure mentioned above.

Electrochemistry and Product Analyses.

Electrochemical reduction of CO_2 was performed in an H-type cell with an Ag/AgCl reference electrode and Pt wire as the counter electrode. The cathode and anode compartments were separated by a cation exchange membrane (Nafion 117). 0.5 M (60 mL) $KHCO_3$ aqueous solution was used as the electrolyte. Before electrolysis, the electrolyte was pre-saturated with CO_2 by bubbling the gas for 30 min (pH 7.4). Current densities were calculated based on the geometric area of the working electrode. A CHI660E electrochemical workstation was used for the electrochemical studies.

Electrochemical behaviors were evaluated by the characterization of cyclic voltammetry and chronopotentiometry. All potentials were referred to a reversible hydrogen electrode (RHE).

The gas chromatograph (GC, SP-6890) is equipped with columns of TDX-01, GDX502, and PEG-20M, detectors of thermal conductivity detector (TCD) and flame ionization detector (FID) with Ar as a carrier gas. The gaseous products were drawn from the headspace by a gas-tight syringe and injected into the GC. H_2, CO and CO_2 with significant amounts are detected by TCD. FID is used to detect a trace of hydrocarbon products. Standard curves for H_2 and CO are shown in Figure S10. Liquid phase products of methanol and ethanol were detected by the FID after eluting from the PEG-20M column (Figure S11). The liquid phase product of $COOH^-$ was quantified using a high-end ion chromatography system (ICS-2000, DIONEX). The standard curve for $COOH^-$ is shown in Figure S12.

Additional characterizations of the electrode were obtained with scanning electron microscopy (SEM) (S-4800II, Japan) and powder X-ray diffraction (PXRD) measurement (AXS D8 ADVANCE, Bruker, German). Low-pressure N_2 adsorption measurements (up to 1 bar) were performed on a Micromeritics ASAP 2020 HD88 surface area and a pore size analyzer. The surface elemental compositions of the samples were investigated by X-ray photoelectron spectroscopy (XPS, ESCALAB 250Xi, Thermo Scientific, America). The Fourier transform infrared spectra of the catalysts are collected on Vertex 70 v, Bruker. The UV absorption characteristics were measured on a Cary 5000 UV spectrophotometer. The CO_2 capture of each catalyst is tested by thermogravimetric analyzer (STA 449 F3).

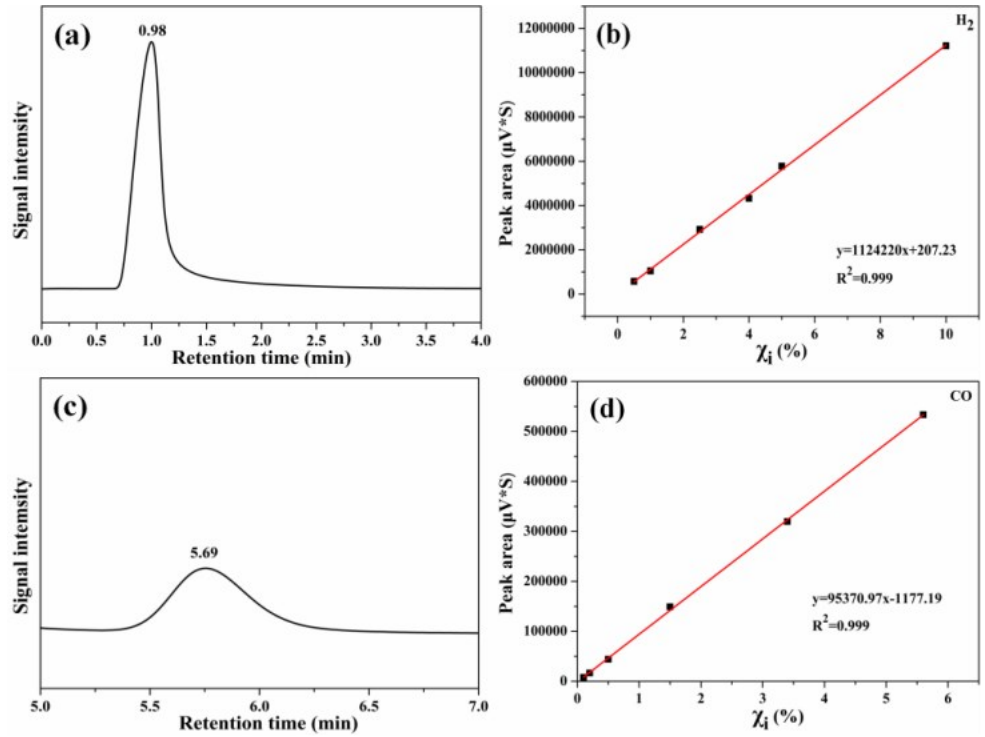

Figure S10. Chromatographic peak and standard curve for pure hydrogen and CO established on TDX-01 column for GC analysis.

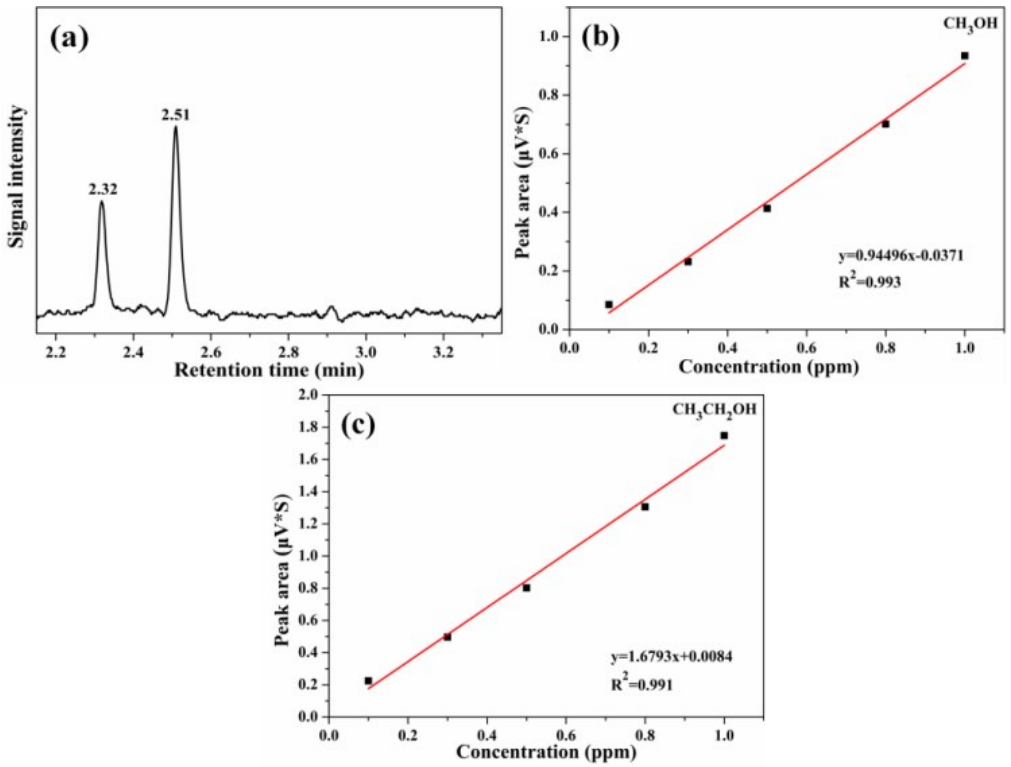

Figure S11. Chromatographic peaks and standard curves for pure methanol and ethanol established on PEG-20M column for GC analysis.

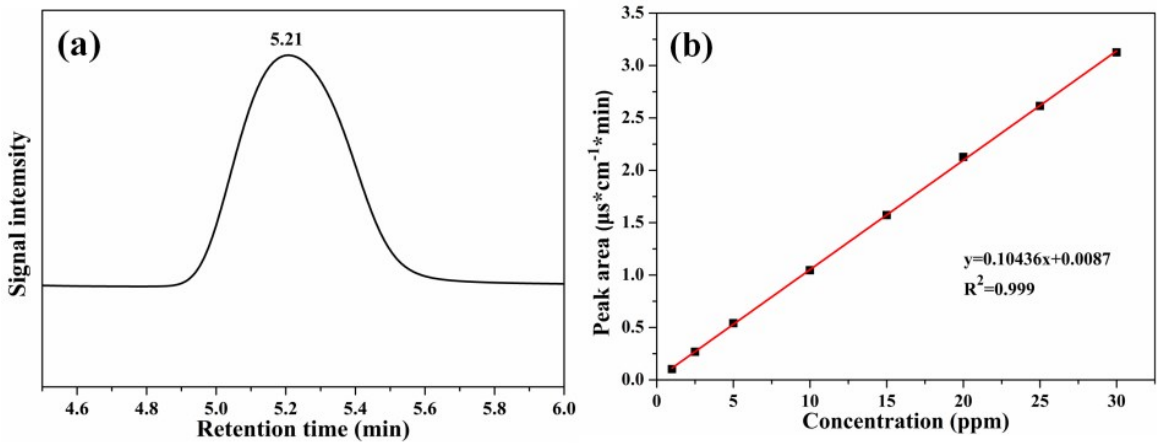

Figure S12. Chromatographic peak and standard curve for $COOH^-$ established on high-end ion chromatography.

References

1 H. Q. Xu, J. H. Hu, D. K. Wang, Z. H. Li, Q. Zhang, Y. Luo, S. H. Yu and H. L. Jiang, *J. Am. Chem. Soc.*, 2015, **137**, 13440–13443.

2 N. Sharma, S. S. Dhankhar and C. M. Nagaraja, *Sustain. Energy Fuels.*, 2019, **3**, 2977–2982.

3 R. Hinogami, S. Yotsuhashi, M. Deguchi, Y. Zenitani, H. Hashiba and Y. Yamada, *ECS Electrochem. Lett.*, 2012, **1**, H17–H19.

4 C. W. Kung, C. O. Audu, A. W. Peter, H. Noh, O. K. Farha and J. T. Hupp, *ACS Energy Lett.*, 2017, **2**, 2394–2401.

5 T. N. Huan, E. S. Andreiadis, J. Heidkamp, P. Simon, E. Derat, S. Cobo, G. Royal, A. Bergmann, P. Strasser, H. Dau, V. Artero and M. Fontecave, *J. Mater. Chem. A*, 2015, **3**, 3901–3907.

6 S. Sen, D. Liu and G. T. R. Palmore, *ACS Catal.*, 2014, **4**, 3091–3095.

7 J. Chung, D. H. Won, J. Koh, E. H. Kim, S. I. Woo, *Phys. Chem. Chem. Phys*., 2016, **18**, 6252–6258.

8 K. Gupta, M. Bersani and J. A. Darr, *J. Mater. Chem. A*, 2016, **4**, 13786–13794.

9 Y. X. Duan, F. L. Meng, K. H. Liu, S. S. Yi, S. J. Li, J. M. Yan and Q. Jiang, *Adv. Mater.*, 2018, **30**, 1706194.

10 Z. Weng, Y. S. Wu, M. Y. Wang, J. B. Jiang, K. Yang, S. J. Huo, X. F. Wang, Q. Ma, G. W. Brudvig, V. S. Batista, Y. Y. Liang, Z. X. Feng and H. L. Wang, *Nat. Commun*., 2018, **9**,

415–423.

11 J. X. Wu, S. Z. Hou, X. D. Zhang, M. Xu, H. F. Yang, P. S. Cao and Z. Y. Gu, *Chem. Sci.*, 2019, **10**, 2199.

12 K. Zhao, Y. M. Liu, X. Quan, S. Chen and H. T. Yu, *ACS Appl. Mater. Interfaces.*, 2017, **9**, 5302–5311.

13 Y. Hori, A. Murata, R. Takahashi and S. Suzuki, *J. Chem. Soc. Chem. Commun.*, 1988, **1**, 17–19.

14 Y. Hori, A. Murata and R. Takahashi, *J. Chem. Soc. Faraday Trans.*, 1989, **1**, **85**, 2309–2326.

15 Y. Huang, A. D. Handoko, P. Hirunsit and B. S. Yeo, *ACS Catal.*, 2017, **7**, 1749–1756.

16 C. W. Li and M. W. Kanan, *J. Am. Chem. Soc.*, 2012, **134**, 7231–7234.

17 P. Huang, S. Q. Ci, G. X. Wang, J. C. Jia, J. W. Xu and Z. H. Wen, *J. CO_2 UTIL.*, 2017, **20**, 27–33.

18 B. C. Marepally, C.;Ampelli, C. Genovese, F. Tavella, L. Veyre, E. A. Quadrelli, S. Perathoner and G. Centi, *J. CO_2 UTIL.*, 2017, **21**, 534–542.

19 S. J. Guo, S. Q. Zhao, J. Gao, C. Zhu, X. Q. Wu, Y. J. Fu, H. Huang, Y. Liu and Z. H. Kang, *Nanoscale.*, 2017, **9**, 298–304.

20 L. Li, F. F. Cai, F. X. Y. Qi and D. K. Ma, *J. Alloys Compod.*, 2020, **841**, 155789.

21 X. W. An, S. S. Li, X. Q. Hao, X. Du, T. Yu, Z. D. Wang, X. G. Hao, A. Abudula and G. Q. Guan, *Sustain. Energy Fuels*, 2020, **4**, 2831–2840.

22 K. Ye, A. Cao, J. Q. Shao, G. Wang, R. Si, N. Ta, J. Q. Xiao and G. X. Wang, *Sci. Bull.*, 2020, **65**, 711–719.

23 W. Ni, C. X. Li, X. G. Zang, M. Xu, S. L. Huo, M. Q. Liu, Z. Y. Yang and Y. M. Yan, *Appl. Catal. B*, 2019, **259**, 118044.

24 X. W. An, S. S. Li, A. Yoshida, T. Yu, Z. D. Wang, X. G. Hao, A. Abudula and G. Q. Guan, *ACS Appl. Mater. Interfaces*, 2019, **11**, 42114–42122.

25 M. H. Zhu, P. F. Tian, J. Y. Li, J. C. Chen, J. Xu and Y. F. Han, *Chem. Sus. Chem.*, 2019, **12**, 3955–3959.

26 S. Ajmal, Y. Yang, K. J. Li, M. A. Tahir, Y. Y. Liu, T. Wang, A. U. R. Bacha, Y. Q. Feng, Y. Deng and L. W. Zhang, *J. Phys. Chem. C*, 2019, **123**, 11555–11563.

27 Y. S. Zhang, Z. Cai, Y. X. Zhao, X. M. Wen, W. W. Xu, Y. Zhong, L. Bai, W. Liu, Y. Zhang, Y. Zhang, Y. Kuang and X. M. Sun, *Nanoscale Horiz*., 2019, **4**, 490–494.

28 Y. T. Wang, H. J. Hu, Y. F. Sun, Y. Tang, L. M. Dai, Q. Hu, A. Fisher and X. J. Yang, *Adv. Mater. Interfaces*, 2018, **6**, 1801200.

29 H. J. Hu, Y. Tang, Q. Hu, P. Y. Wan, L. M. Dai and X. J. Yang, *Appl. Surf. Sci*., 2018, **445**, 281–286.

30 D. W. Feng, W. C. Chung, Z. W. Wei, Z. Y. Gu, H. L. Jiang, Y. P. Chen, D. J. Darensbourg and H. C. Zhou, *J. Am. Chem. Soc.*, 2013, **135**, 17105–17110.

31 D. W. Feng, Z. Y. Gu, J. R. Li, H. L. Jiang, Z. W. Wei and H. C. Zhou, *Angew. Chem. Int. Ed*., 2012, **124**, 10453–10456.